Current Research in Materials Chemistry

# Type-II Heterojunctions in $SnO_2$-Coated $TiO_2$ Core-Shell Nanoparticles

**Riddhiman Medhi[1], Nhat M. Ngo[1], Tai-Chou Lee[2], and T. Randall Lee[1*]**

[1]*Department of Chemistry and the Texas Center for Superconductivity, University of Houston, 4800 Calhoun Road, Houston, Texas 77204-5003, United States.*

[2] *Department of Chemical and Materials Engineering, National Central University, 300 Jhongda Road, Jhongli City 32001, Taiwan.*

**Article Details**

Article Type: Research Article
Received date: 04th October, 2021
Accepted date: 27th December, 2021
Published date: 29th December, 2021

[*]**Corresponding Author:** Lee, T. R., Ph.D., Cullen Distinguished University Chair & Associate Dean for Research, College of Natural Sciences and Mathematics, University of Houston, TX 77204-5003. United States. E-mail: trlee@uh.edu

**Citation:** Medhi, R., Ngo, N. M., Lee, T.C., Lee,T. R. (2021). Type-II Heterojunctions in $SnO_2$-Coated $TiO_2$ Core-Shell Nanoparticles. *Cur Res Mater Chem 3*(1): 112. doi: https://doi.org/10.33790/crmc1100112.



## Abstract

Titanium dioxide ($TiO_2$) and tin oxide ($SnO_2$) are two popular wide band-gap semiconductors for photocatalytic and electronic applications such as solar cells, optoelectronic devices, and lithium-ion batteries. Nanosized $TiO_2$ structures have strong absorption in the UV region while $SnO_2$ is a powerful transparent conducting oxide. Composites of $TiO_2$ and $SnO_2$ are especially attractive since they form a type-II heterojunction extending the lifetime of charge carriers and enhancing photoconversion efficiency. In this study, the synthesis of $TiO_2$ nanoparticles as well as their uniform and controlled coating with $SnO_2$ shells are described, providing the first utilization of sodium stannate to grow $SnO_2$ shells on a metal-oxide core. The step-growth method utilized here shows the ability to vary the shell thickness between 5-40 nm while maintaining uniformity of the shell. As such, the complete synthesis route involves facile and reproducible surfactant-free solution-based methods at moderate temperatures. The nanoparticles were characterized using scanning electron microscopy (SEM), transmission electron microscopy (TEM), X-ray photoelectron spectroscopy (XPS), energy-dispersive X-ray spectroscopy (EDX), and X-ray diffraction (XRD). Overall, this paper represents reliable nanoscale fabrication techniques offering key advancements in photovoltaic and optoelectronic applications.

**Keywords:** $TiO_2$, $SnO_2$, Heterojunction, Core-shell, Nanoparticles, Wide Band-gap Semiconductor

## Introduction

Metal oxides have emerged as an important class of compounds for photovoltaics, optoelectronics, and photocatalysis [1–9]. Metal oxide semiconductors with a wide band gap (2-4 eV) have been used for the fabrication of solar cells, lithium-ion batteries, thin-film transistors (TFTs), piezoelectric devices, light-emitting diodes (LEDs), integrated circuits, chemical sensors, and biosensors [1–7,10]. The fabrication of nanoscale colloidal particles of metal oxides is important to improve cost-efficiency and to enhance our ability to control optical and electrical properties at the nanoscale [8]. In recent times, metal oxide nanoparticles have been shown to be effective materials for photocatalytic and photovoltaic applications via the utilization of solar energy [5,8]. The band energies of the metal oxides play a critical role in the design of effective photocatalysts and photovoltaic solar cells. Among the metal oxides, titanium dioxide ($TiO_2$) is the most widely investigated metal oxide photocatalyst due to its relatively low cost, high absorption, low toxicity, and stability [11]. However, $TiO_2$ suffers from poor quantum yields caused by rapid recombination of photogenerated electrons and holes [11–13]. In recent times, nanoscale metal oxide heterojunctions have garnered special attention due to the ability to compensate for the electronic limitations of metal oxides. The band energies of the metal oxides can be aligned with others to promote specific electronic processes, while suppressing others. The $SnO_2$/$TiO_2$ heterojunction has emerged as a powerful system to enhance the properties of either oxide in photocatalytic and photovoltaic applications [14–17].

$SnO_2$ and $TiO_2$ have similar crystal structures (rutile and anatase) with comparable lattice constants (a = 4.5–4.8 A˚, c = 2.9–3.2 A˚ for rutile; a = 3.7–4.0 A˚, c = 9.6–10.2 A˚ for anatase) and comparable band gaps (~3.2–3.6 eV) [18]. However, these structural similarities do not translate to similarities in their optical and electronic properties. On analyzing the electronic structure of the two oxides, their photovoltaic compatibility becomes evident. $TiO_2$ shows several energetically flat and close-lying levels in the conduction band (CB). $SnO_2$, on the other hand, has a single highly dispersive level in its CB [18]. As a consequence, $TiO_2$ favors a much stronger optical absorption in the UV, while $SnO_2$ is a much better conductor of the electrons in its CB. More importantly, the combination of $SnO_2$ and $TiO_2$ form a type-II heterojunction. The CB of $TiO_2$ is positioned above the CB of $SnO_2$, while the valence band (VB) of $TiO_2$ is energetically positioned between the VB and CB of $SnO_2$ [19]. As a consequence of this staggered conformation of energy levels, the CB of $SnO_2$ acts as a sink for photogenerated electrons from $TiO_2$, while the photogenerated holes of $SnO_2$ move in the opposite direction and accumulate in the VB of $TiO_2$. These phenomena lead to an excitonic charge separation state that prolongs the lifetime of the charge carriers [20]. These features make the $TiO_2$/$SnO_2$ core-shell heterojunction extremely effective for dye-sensitized solar cells and photoelectrochemical cells [14–16]. Electron trapping in the CB of $SnO_2$ also leads to effective inhibition of back-electron transfer (BET) between the oxidized dye and reduced semiconductor in dye-sensitized solar cells [14–16].

Until now, such $TiO_2$/$SnO_2$ heterojunctions have been mostly generated in thin films, nanofibers, and nanowire arrays – structures that lack morphological uniformity on the nanoscale [19,21]. Herein, we describe a controllable strategy to synthesize this heterojunction

in a colloidal nanoparticle. The nanoparticles reported herein employ a $SnO_2$ coating around a $TiO_2$-based core, which can concentrate electrons on the surrounding $SnO_2$ shell, making them more effective as photocatalysts. The ability to fabricate $SnO_2$ layers with varying thickness on $TiO_2$ nanoparticles adds a degree of control at the nanoscale never achieved before in such systems and allows us to fine-tune the optical and electrical properties on the nanoscale. All the nanoparticles were characterized by scanning electron microscopy (SEM), transmission electron microscopy (TEM), energy-dispersive X-ray spectroscopy (EDX), X-ray photoelectron spectroscopy (XPS), and X-ray diffraction (XRD).

## Materials and Methods

### Materials

Titanium nitride (TiN) and sodium stannate trihydrate ($Na_2SnO_3.3H_2O$) were purchased from Sigma-Aldrich and used without further purification. Hydrogen peroxide ($H_2O_2$, 30%, Macron Fine Chemicals), ammonium hydroxide ($NH_4OH$, 28–30%, VWR Analytical) and ethanol (EtOH, anhydrous, Flinn Scientific) were purchased from the indicated suppliers and used without modification. Water was purified to a resistance of 18 MΩ-cm (Academic Milli-Q Water System, Millipore Corporation). All glassware and reaction vessels used during the experiments was cleaned twice in an aqua regia solution (3:1 HCl: $HNO_3$), rinsed with water and acetone, and then dried in the oven prior to each use. After repeated use, the glassware was also occasionally cleaned in a base bath followed by piranha solution (3:1 $H_2SO_4$:$H_2O_2$) and then again by aqua regia.

### Characterization Methods

A LEO-1525 scanning electron microscope (SEM) was used to image the nanoparticles with an accelerating voltage of 15 kV. All SEM samples were prepared by depositing on a silicon wafer, pre-cleaned with water and ethanol. Size distribution analysis was performed based on SEM images of 50 nanoparticles for each sample using ImageJ, to determine the average diameters. Shell thicknesses were calculated using equation 1; where $D_{Avg(core\text{-}shell)}$ = average diameter for $TiO_2$@$SnO_2$ nanoparticles and $D_{Avg(core)}$ = average diameter of $TiO_2$ nanoparticles:

$$\text{Shell thickness} = D_{Avg(core\text{-}shell)} - D_{Avg(core)} \quad /2 \qquad (1)$$

The nanoparticles were also imaged using a JEM-2010 FX transmission electron microscope (TEM) and operating at an accelerating voltage of 200 kV. All TEM samples were deposited on 300 mesh holey carbon-coated copper grids and dried overnight before analysis. Energy-dispersive X-ray spectroscopy (EDX) data were collected by an EDX attached to the JEM-2010 TEM instrument, providing the elemental composition of the particles. X-ray diffraction (XRD) patterns for the nanoparticles were obtained using a X'PERT PRO PANalytical X-ray diffractometer. A glass slide was cleaned with piranha and a concentrated sample of the nanoparticles in water was deposited onto the cleaned glass slides. The XRD data were obtained using Cu Kα radiation over the 2θ range of 10°–80° over 15 minutes. A PHI 5700 X-ray photoelectron spectrometer X-ray photoelectron was used to collect spectroscopy (XPS) data. A monochromatic Al Kα source with 10 mA emission current and 15kV emission bias was used as the measurement parameters. Concentrated samples of the nanoparticles in water were dropped on copper-tape-covered silicon wafers. Before sample preparation, the copper-tape-covered slides were washed with Milli-Q water followed by ethanol and dried with nitrogen gas. UV-Vis extinction spectra were obtained using a Cary 50 Scan UV-vis spectrometer.

### Synthesis of $TiO_2$ Nanoparticles ($TiO_2$ NPs)

The first step in the synthesis of $TiO_2$ nanoparticles involved the preparation of a Ti-peroxo complex. Specifically, the TiN (0.10 g) was dispersed in 100 mL of Millipore water followed by the addition of 10 mL of 30% hydrogen peroxide ($H_2O_2$) and 10 mL of 25% ammonia solution. A transparent yellow solution of Ti-peroxo complex was obtained after 2 h of stirring at room temperature. An aliquot of the Ti-peroxo complex solution was mixed with ethanol (1:2 volume ratio) under vigorous stirring at 80 °C. After heating for 20 h, the solution was cooled to room temperature and centrifuged to collect a white precipitate of amorphous $TiO_2$ particles. The precipitate was washed with ethanol and redispersed in 30 mL of ethanol. Anatase phase $TiO_2$ nanoparticles were obtained by hydrothermal heating of the dried nanoparticles in a Teflon-lined autoclave at 200 ºC for 24 h. These particles were also later collected by centrifugation and redispersed in an equivalent amount of ethanol as the starting solution.

### Synthesis of $SnO_2$-Coated $TiO_2$ Nanoparticles – Routes A, B, C ($TiO_2$@$SnO_2$-A/B/C)

For Route A, in a 20-mL glass vial, 1 mL of $TiO_2$ NPs from the previous step (~0.004 g of $TiO_2$ NPs) were taken as is, and 9 mL of Milli-Q water was added. The solution was sonicated in an ultrasonic bath for 10 min. The reaction mixture was then heated to 80 ºC. Subsequently, 1 mL of a 0.04 M sodium stannate solution was added to the vial, and the reaction was continued at 80 ºC for 20 min to generate the sample $TiO_2$@$SnO_2$-A. The nanoparticles were collected by centrifugation at 6000 rpm for 20 min, the supernatant was discarded to remove any remaining water and then finally redispersed in 1 mL of Milli-Q water.

Similarly for Route B, 1 mL of $TiO_2$ NPs from the previous step (~0.004 g of $TiO_2$ NPs) were taken as is, and 9 mL of Milli-Q water was added. After sonication for 10 min, the reaction mixture was heated to 80 ºC. Subsequently, 1 mL of a 0.2 M sodium stannate solution was added to the vial, and the reaction was continued at 80 ºC for 20 min to generate the sample $TiO_2$@$SnO_2$-B.

For Route C, in a 20-mL glass vial, 1 mL of $TiO_2$ NPs (~0.004 g of $TiO_2$ NPs) from the previous step were taken as is, and 4 mL of Milli-Q water was added. After sonication for 10 min, the reaction mixture was heated to 80 ºC. Subsequently, 1 mL of a 0.08 M sodium stannate solution was added to the vial, and the reaction was continued at 80 ºC for 20 min to generate the sample $TiO_2$@$SnO_2$-C.

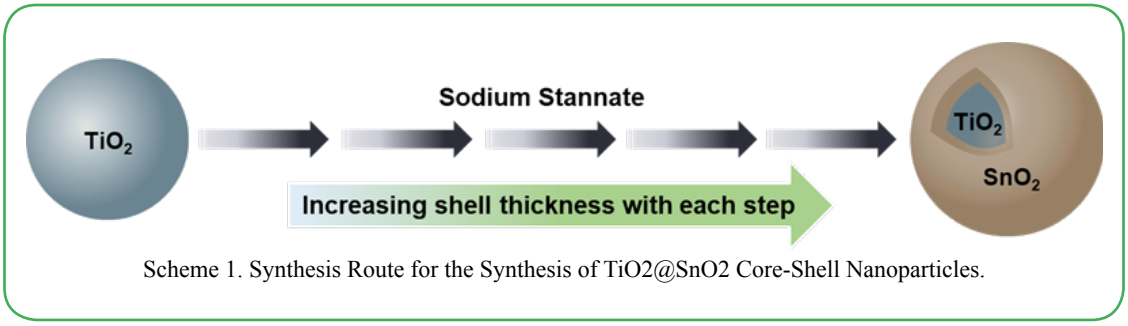


Scheme 1. Synthesis Route for the Synthesis of TiO2@SnO2 Core-Shell Nanoparticles.

**Synthesis of $SnO_2$-Coated $TiO_2$ Nanoparticles – Route D ($TiO_2$@$SnO_2$-D)**

In a 20-mL glass vial, 1 mL of $TiO_2$ NPs from the previous step (~0.004 g of $TiO_2$ NPs) were taken as is, and 4 mL of Milli-Q water was added. The solution was sonicated in an ultrasonic bath for 10 min. The reaction mixture was then heated to 80 ºC. Subsequently, 200 µL of a 0.04 M sodium stannate solution was added to the vial, and the reaction was continued at 80 ºC for 20 min to generate the sample $TiO_2$@$SnO_2$-D1. To synthesize $TiO_2$@$SnO_2$-D2, another 200 µL of a 0.04 M sodium stannate solution was added to the vial, and the reaction was continued at 80 ºC for an additional 20 min. This addition process was repeated for three times to generate $TiO_2$@$SnO_2$-D3, $TiO_2$@$SnO_2$-D4, and $TiO_2$@$SnO_2$-D5, respectively. The target sample was extracted by centrifugation at 6000 rpm for 20 min, the supernatant was discarded to remove any remaining water and then finally redispersed in 1 mL of Milli-Q water.

**Synthesis of $SnO_2$-Coated $TiO_2$ Nanoparticles – Route E ($TiO_2$@$SnO_2$-E)**

In a 20-mL glass vial, 1 mL of $TiO_2$ NPs from the previous step (~0.004 g of $TiO_2$ NPs) were taken as is, and 4 mL of Milli-Q water was added. The solution was sonicated in an ultrasonic bath for 10 min. The reaction mixture was then heated to 80 ºC. Subsequently, 200 µL of a 0.08 M sodium stannate solution was added to the vial, and the reaction was continued at 80 ºC for 20 min to generate the sample $TiO_2$@$SnO_2$-E1. To synthesize $TiO_2$@$SnO_2$-E2, another 200 µL of a 0.08 M sodium stannate solution was added to the vial, and the reaction was continued at 80 ºC for an additional 20 min. This addition process was repeated for three times to generate $TiO_2$@$SnO_2$-E3, $TiO_2$@$SnO_2$-E4, and $TiO_2$@$SnO_2$-E5, respectively. The target sample was extracted by centrifugation at 6000 rpm for 20 min, the supernatant was discarded to remove any remaining water, and then finally redispersed in 1 mL of Milli-Q water.

**Synthesis of $SnO_2$-Coated $TiO_2$ Nanoparticles – Route F ($TiO_2$@$SnO_2$-F)**

In a 20-mL glass vial, 1 mL of $TiO_2$ NPs from the previous step (~0.004 g of $TiO_2$ NPs) were taken as is, and 4 mL of Milli-Q water was added. The solution was sonicated in an ultrasonic bath for 10 min. The reaction mixture was then heated to 80 ºC. Subsequently, 1 mL of a 0.04 M sodium stannate solution was added to the vial and the reaction was continued at 80 ºC for 20 min. This generates the sample $TiO_2$@$SnO_2$-F1. To synthesize $TiO_2$@$SnO_2$-F2, another 1 mL of a 0.04 M sodium stannate solution was added to the vial and the reaction was continued at 80 ºC for an additional 20 min. This addition process was repeated for three times to generate $TiO_2$@$SnO_2$-F3, $TiO_2$@$SnO_2$-F4, and $TiO_2$@$SnO_2$-F5, respectively. The target sample was extracted by centrifugation at 6000 rpm for 20 min, the supernatant was discarded to remove any remaining water and then finally redispersed in 1 mL of Milli-Q water.

## Results And Discussion

**Synthesis and Morphological Study of the Nanoparticles**

*$TiO_2$ Nanoparticles ($TiO_2$ NPs)*

Titanium dioxide nanoparticles were synthesized according to a previously reported method [22]. Briefly, TiN was oxidized by $H_2O_2$ and treated under alkaline conditions to yield a stable Ti precursor in the form of a Ti-peroxo complex $[Ti(OH)_3O_2]$-. This Ti-peroxo complex slowly precipitated as $TiO_2$ seeds in ethanol, which then grew to form $TiO_2$ nanoparticles. The SEM image in Figure 1a shows that the final $TiO_2$ nanoparticles are spherical and well dispersed. Size distribution analysis showed the average diameter of the nanoparticles to be 116 ± 43 nm.

*$SnO_2$-Coated $TiO_2$ Nanoparticles ($SnO_2$@$TiO_2$)*

After the successful synthesis of the $TiO_2$ NPs, tin oxide shells were grown around these nanoparticles, as outlined in Scheme 1. The synthesis strategy to grow the $SnO_2$ shells is loosely based on the method reported by Medhi et al [23]. The $SnO_2$ shells were formed by using an aqueous sodium stannate trihydrate precursor solution. $SnO_2$ can be spontaneously formed from an aqueous solution of sodium stannate when the pH is lowered to < 11 [24-26]. Crystalline $SnO_2$ is the most stable phase at pH values under 11.7 [25]. The pH was controlled by heating the temperature of the reaction mixture containing the nanoparticle cores to 80 ºC [26]. The addition of aqueous sodium stannate solution to this reaction mixture led to the spontaneous formation of $SnO_2$ crystallites around the $TiO_2$ NPs.

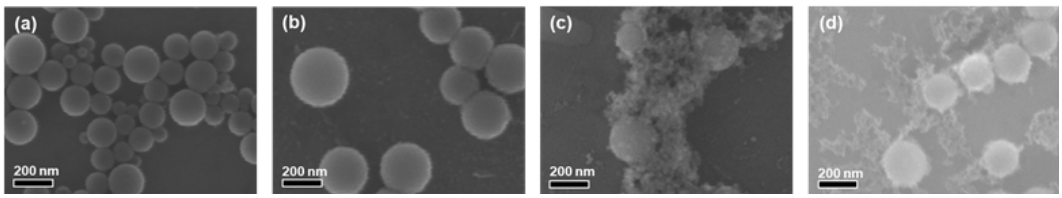


Figure 1. SEM images of (a) $TiO_2$, and (b–d) $TiO_2$@$SnO_2$ nanoparticles synthesized via Routes A, B, and C, respectively.

It is important to note that, in the absence of a nanoparticle core, the sodium stannate crystallizes to form free $SnO_2$ nanoparticles with diameters of ~30 nm [24]. Hence, it is important to adjust the concentration of the nanoparticle core and the precursor feed. In this study, a variety of reaction conditions were explored. In the first iteration (Route A), 1 mL of $TiO_2$ NPs was diluted to 10 mL, heated to 80 ºC, and 1 mL of 0.04 M sodium stannate solution was added at once and allowed to react for 20 min. No tin oxide shells were observed in the SEM images, as shown Figure 1b. In the second iteration (Route B), 1 mL of $TiO_2$ NPs was similarly diluted to 10 mL, and 1 mL of a more concentrated 0.2 M sodium stannate solution was added. In this case, many free $SnO_2$ NPs were obtained, with a limited number of $SnO_2$ crystallites forming shells around the $TiO_2$ NPs (see Figure 1c). In the third iteration (Route C), the 1 mL of $TiO_2$ NP solution was diluted to just 5 mL, and 1 mL of 0.08 M sodium stannate solution was added. The doubled concentration of $TiO_2$ nanoparticle cores was anticipated to facilitate the localization of $SnO_2$ crystallites at the surface of the $TiO_2$ cores. Although the number of free $SnO_2$ NPs decreased, there was still no significant shell growth on the surface of the $TiO_2$ NPs (see Figure 1d). Typically, in previous studies with metal nanoparticle cores, sodium stannate has been added in a single injection [23,27]. The sodium stannate has been observed to preferentially crystallize as $SnO_2$ on the surface of Au NPs. However, the Au NPs in those studies were stabilized by citrate ions, which have an affinity towards $SnO_2$ and most likely assist the localization of the initial $SnO_2$ crystallites on the surface of the Au NPs and subsequent growth of a complete $SnO_2$ shell. However, the $TiO_2$ NPs in the present study were not stabilized by any surfactant or ligand. Thus, the $TiO_2$ NP core surface lacks any inherent affinity to localize the $SnO_2$ crystallites. A different approach is therefore required for the controlled growth of $SnO_2$ shells on these $TiO_2$ cores.

In the fourth iteration (Route D), the 1 mL of $TiO_2$ NPs were diluted to 5 mL, and 1 mL of 0.08 M sodium stannate solution was added in five different steps of 200 µL each and stirred for 20 min at 80 ºC for each step. The SEM images of the nanoparticles after each stepwise reaction are presented in Figure 2. As illustrated in the SEM images in Figure 2, no significant shell growth was observed till the third step (a total 0.6 mL of 0.08 M sodium stannate), although no free $SnO_2$ NPs were observed either. After the fourth step, the surface of the initially smooth $TiO_2$ NPs begins to become rugged due to the growth of $SnO_2$ crystallites, as shown in Figure 2e. Size distribution analysis shows a shell thickness of 4 ± 2 nm. The SEM image of the nanoparticles after the fifth step of sodium stannate addition is mostly like the fourth step, with the appearance of rugged surfaces indicating the growth of an $SnO_2$ shell (see Figure 2f). Size distribution analysis showed a calculated shell thickness of 12 ± 7 nm. Notably, the total amount of sodium stannate added after the fifth step in Route A was the same as Route C (total 1 ml of 0.08 M), but the stepwise addition significantly reduced the number of free tin oxide nanoparticles in solution (see Figures 1d and 2f).

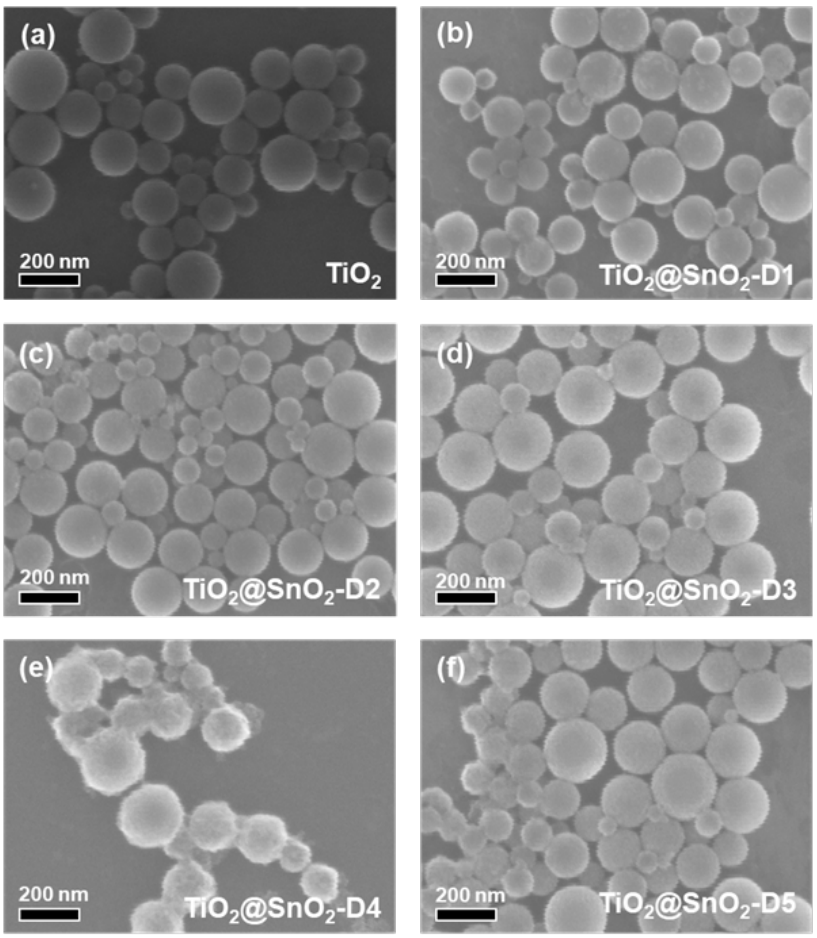


Figure 2. SEM images of (a) $TiO_2$, and (b–d) $TiO_2$@$SnO_2$-D nanoparticles after each step of coating via Route D.

To increase the thickness of the $SnO_2$ shell, the fifth iteration (Route E) utilized 1 mL of $TiO_2$ NPs diluted to 5 mL and 1 mL of 0.04 M sodium stannate solution was added in five different steps of 200 µL each, and stirred for 20 min at 80 ºC for each step. As shown in the SEM images in Figure 3b, no significant shell growth was observed after the first step. However, after the second step, the $SnO_2$ shell was discernable on the surface of the $TiO_2$ NPs, which corresponds well with $TiO_2$@$SnO_2$-D4, which utilized equivalent moles of sodium stannate. Although this iteration uses more concentrated solution of sodium stannate, no free $SnO_2$ nanoparticles were observed. The calculated shell thickness of 9 ± 4 nm is greater than that observed for $TiO_2$@$SnO_2$-D4 (4 ± 2 nm). The $SnO_2$ shells became thicker and more evident with each subsequent step of adding 0.04 M sodium stannate as observed with $TiO_2$@$SnO_2$-E3, $TiO_2$@$SnO_2$-E4, and $TiO_2$@$SnO_2$-E5 in Figures 3d–f, with a shell thickness of 12 ± 1 nm, 30 ± 5 nm, 30 ± 3 nm, respectively. Notably, with this stepwise addition, no free $SnO_2$ NPs were observed after adding the full 1 mL of 0.04 M sodium stannate, which is a stark difference to adding the same and even smaller amounts of sodium stannate in the first and third iterations (Routes A and C). As such, this route outlines a reliable strategy to localize the growth of $SnO_2$ shells on $TiO_2$ cores. Moreover, to our knowledge, this is the first time a $SnO_2$ shell has been synthesized with a thickness >20 nm. Typically, due to the single-injection method employed previously, attempts to increase shell thickness by increasing the concentration of sodium stannate precursor spontaneously led to the formation of free $SnO_2$ NPs instead of increased shell thicknesses.

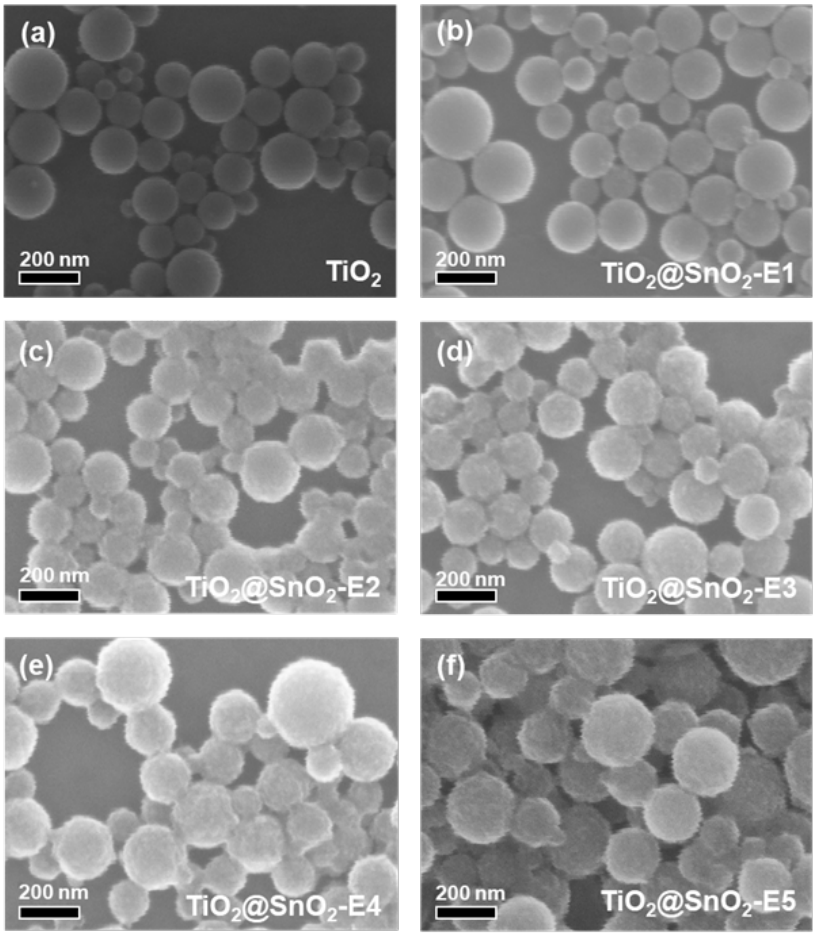


Figure 3. SEM images of (a) $TiO_2$, and (b–d) $TiO_2$@$SnO_2$-E nanoparticles after each step of coating via Route E.

To explore if the shell thickness could be further increased, the sixth iteration (Route F) utilized 1 mL of $TiO_2$ NPs diluted to 5 mL, and 5 mL of 0.04 M sodium stannate solution was added in five different steps of 1 mL each and stirred for 20 min at 80 ºC for each step. At the first step, the amount of sodium stannate added was the same as that used for $TiO_2$@$SnO_2$-E5. Although no free $SnO_2$ NPs were observed, the $SnO_2$ shells on the surface of the $TiO_2$ in $TiO_2$@$SnO_2$-F1 (Figure 4b) do not appear as thick as those in $TiO_2$@$SnO_2$-E5 (Figure 3f). Size analysis confirmed this observation with a shell thickness of 14 ± 5 nm, considerably lower than the 30 ± 5 nm observed for $TiO_2$@$SnO_2$-E5. After the second step of addition, the $SnO_2$ shells became considerably thicker around the $TiO_2$ cores (Figure 4c), with a thickness of 42 ± 4 nm. The shells appear to further increase in thickness after the third step (Figure 4d), although one can observe a tendency to form bridges consisting of $SnO_2$ particulates between the coated nanoparticles. However, the excess $SnO_2$ crystallites appeared to grow as extensions from the shells rather than as free $SnO_2$ NPs growing from solution as observed with Routes A, B, and C. This trend continued in the fourth and fifth step (Figures 4e,f), wherein the excess $SnO_2$ crystallites progressed from forming bridges to forming a full network mesh of $SnO_2$ engulfing the embedded $TiO_2$ NPs.

The SEM results above demonstrated the most effective shell growth for the $TiO_2$@$SnO_2$-E5 nanoparticles, without forming any bridges, webs, or free $SnO_2$ nanoparticles. This sample was further analyzed by TEM imaging to observe the shell thickness and crystalline composition. The TEM images in Figure 5a and 5b shows the $SnO_2$ shell comprised of minute polycrystallites. This polycrystalline porous nature of the shell is consistent with $SnO_2$ synthesized using the sodium stannate method [23–24,27]. The TEM image in Figure 5a also confirmed that the formation of free $SnO_2$ nanoparticles was limited.

As a whole, these results indicate that once the initial $SnO_2$ crystallites are localized on the surface of the core NPs, the subsequent crystallites also prefer to grow near these initial crystallites forming a shell rather than free nanoparticles in solution. As such, this method establishes a key principle for the controlled growth of $SnO_2$ shells of varying thicknesses around unfunctionalized $TiO_2$ NP cores. Previously, the only method to control $SnO_2$ thickness was to change the amount of sodium stannate solution, with thicknesses varying between 5–12 nm. Even on citrate-stabilized Au NPs, the addition of any more sodium stannate drastically increased the number of free tin oxide NPs while only increasing the shell thickness marginally. Using the step-growth method outlined here should enable the growth of thicker shells in a more controlled fashion even on metal nanoparticle cores.

**Structural Analysis of the Nanoparticles**

Powder XRD analysis was conducted to determine the phases present in the nanoparticles. For the XRD studies, $TiO_2$@$SnO_2$-E5 core-shell nanoparticles were synthesized starting with the hydrothermal heat-treated anatase $TiO_2$ core, since the as-synthesized $TiO_2$-coated nanoparticles show no peaks for $TiO_2$. The XRD pattern for the final core-shell nanoparticles in Figure 6 shows the peaks corresponding to the anatase phase of $TiO_2$ (JCPDS 21-1272) [28].

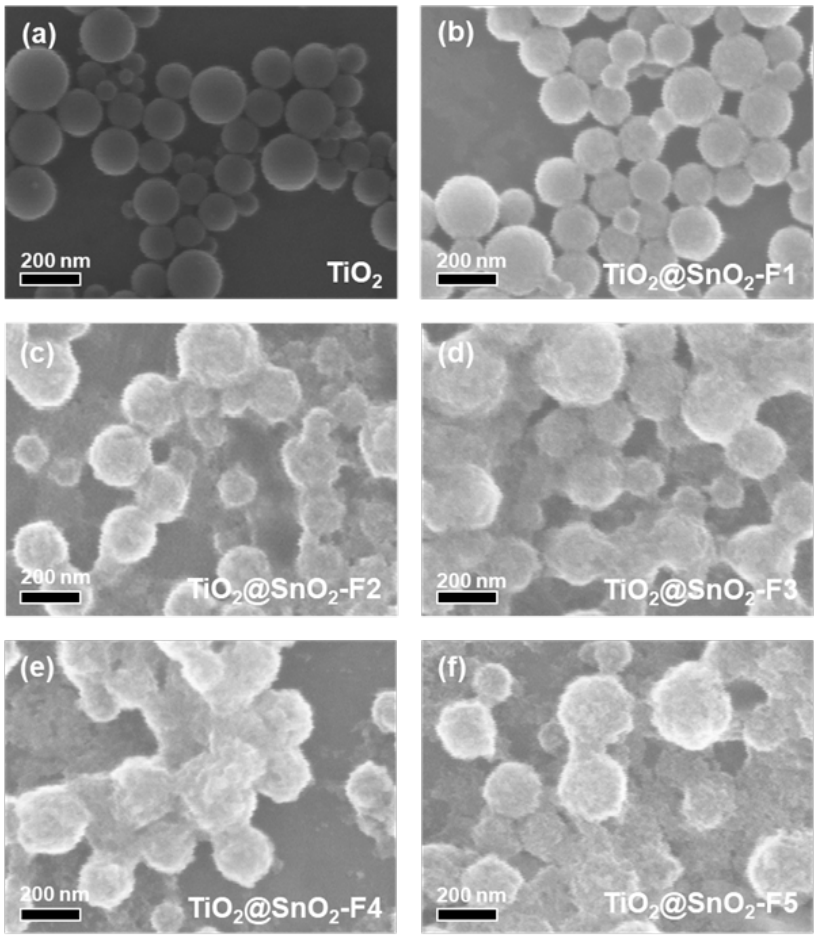


Figure 4. SEM images of (a) TiO2, and (b–d) $TiO_2$@$SnO_2$-E nanoparticles after each step of coating via Route E.

The peaks at 2θ = 25.38, 48.05, 53.95, 55.04, 62.85, and 75.12 respectively correspond to the (101), (200), (105), (211), (204), and (215) planes for anatase $TiO_2$ [29]. Hydrothermal treatment is a standard procedure to achieve anatase phase $TiO_2$ [30]. Interestingly, the $SnO_2$ shells grown atop the anatase $TiO_2$ layer adopt the rutile phase [23–24]. The (110), (101), and (211) peaks observed for the nanoparticles with a $SnO_2$ coating at 2θ = 26.28, 33.71, and 58.51 are characteristic of $SnO_2$ nanoparticles prepared using this method [23–24].

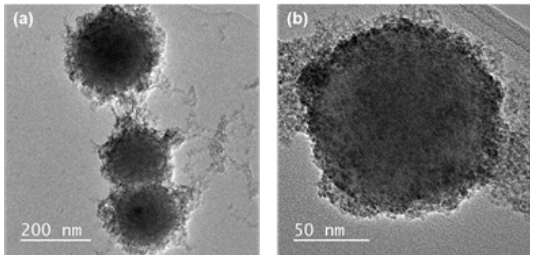


Figure 5. TEM images of $TiO_2$@$SnO_2$-E5 nanoparticles after the fifth step of coating via Route E.

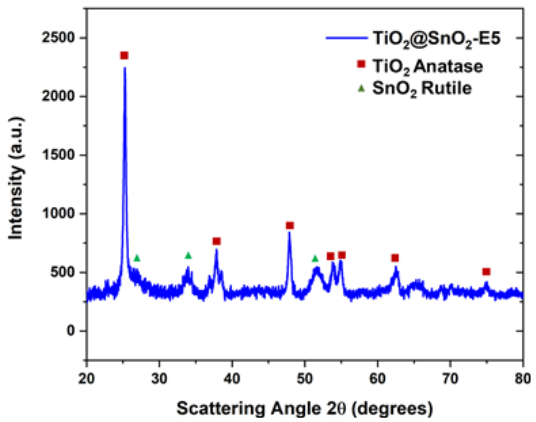


Figure 6. Powder XRD pattern for $TiO_2$@$SnO_2$-E5 nanoparticles.

**Compositional Analysis of the Nanoparticles**

Analysis by XPS was performed to determine the elemental composition on the surface of the nanoparticles at each step of the synthetic process. Figure 7 shows the changes in the elemental composition of the surface after coating with a $SnO_2$ shell. A broad peak at 532 eV for oxygen was observed in the O 1s spectra which is consistent with metal oxides [31]. The peaks for Sn $3d_{5/2}$ and $3d_{3/2}$ at 486.0 eV and 494.5 eV, respectively, can be observed, which confirms the presence of $SnO_2$ [24]. As such, peaks corresponding to Ti $2p_{3/2}$

and $2p_{1/2}$ at 459.0 eV and 464.3 eV, respectively appear even in the coated sample, although the intensity is low [32–33]. It is important to note that XPS is a surface-specific technique and provides the composition at the outer surface of the nanoparticles [34–35]. The intensity for these Sn 3d peaks is much stronger than the Ti 2p peaks, confirming the successful growth of $SnO_2$ shells encapsulating the $TiO_2$ cores. The relative atomic concentrations of all the elements are presented in Figure 7. Even though the relative amount of $TiO_2$ in the nanoparticles was higher than $SnO_2$ (as confirmed by the SEM and TEM images of the core-shell structures and the EDX spectra; vide infra) the relative atomic concentrations derived by XPS were dominated by Sn (13%) vs Ti (7%), which confirmed successful shell growth.

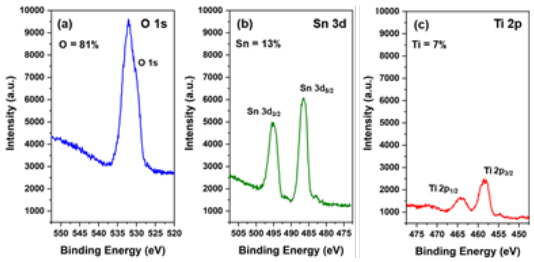


Figure 7. XPS spectra for (a) O 1s region, (b) Sn 3d region, and (c) Ti 2p region for the $TiO_2$@$SnO_2$-E5 nanoparticles.

In addition to XPS, we also performed EDX analysis to further confirm the overall composition of the nanoparticles. Figure 8 shows the EDX spectra for the final core-shell nanoparticle after five rounds of $SnO_2$ coating via Route E. The SEM-EDX spectra show that the nanoparticles contained peaks characteristic for Ti Lα, Kα, and Kβ at 0.45 eV, 4.51 eV, and 4.93 eV, respectively. The characteristic peak for O Kα at 0.53 eV was also visible. The nanoparticles also exhibited the peaks for Sn Lα and Kα at 3.44 eV and 25.27 eV, respectively, arising from the $SnO_2$ shell. The atomic concentrations obtained from the EDX measurements are listed in Figure 8. Oxygendominated the spectra with 86% relative concentration, while Ti constituted 11% and Sn constituted 3%. The relative atomic concentrations of titanium were markedly higher in the EDX measurements compared to the XPS measurements (which mainly probe the surface composition corresponding to the $SnO_2$ shell). These results further confirm that the $TiO_2$ cores are covered by $SnO_2$ shells. The overall relative concentrations of Ti and Sn from EDX also roughly matched the relative dimensions occupied by their corresponding phases in the respective nanoparticle architectures as evaluated from the SEM and TEM images.

In addition to EDX spectroscopy, we also conducted elemental mapping using STEM-EDX to determine the distribution of the elements within the nanoparticles and confirm the core-shell structure. As illustrated in Figure 9, titanium was confined only to the inner regions of the nanoparticles. The distribution of oxygen and tin extended to wider dimensions that covered more of the nanoparticle volume, indicating encapsulation of the $TiO_2$ cores in the nanoparticles. Figure 9 also shows that the distribution of tin extended the widest across the nanoparticle volume, indicating that this element constituted the outermost shell. The oxygen distribution also paralleled the tin distribution, which is consistent with the presence of a $SnO_2$ shell.

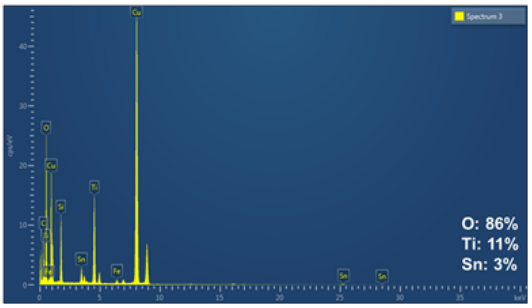


Figure 8. STEM-EDX spectra for $TiO_2$@$SnO_2$-E5 nanoparticles, showing the atomic concentration of the constituent elements O, Ti, and Sn, in the nanoparticles.

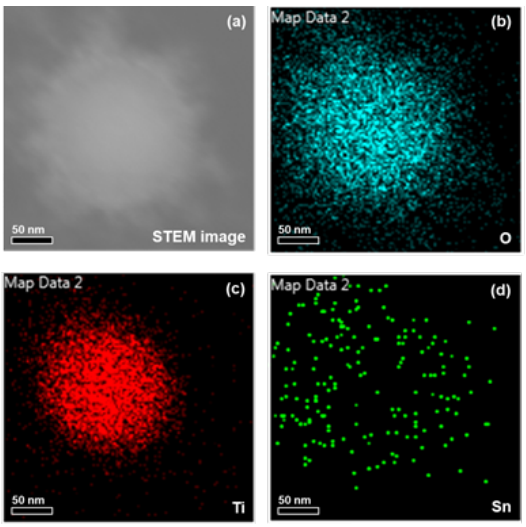


Figure 9. STEM-EDX mapping images of $TiO_2$@ $SnO_2$-E5, showing the distribution of the constituent elements O, Ti, and Sn, within the nanoparticles.

The SEM, XPS, and EDX results confirmed the successful growth of $SnO_2$ shells around the $TiO_2$ cores. This composite design can facilitate the movement of electrons from the CB of $TiO_2$ in the core to the CB of the $SnO_2$ shell, concentrating electrons in the outermost layer. Meanwhile, the holes from the VB of $SnO_2$ can move in the opposite direction toward the VB of $TiO_2$, effectively increasing the separation of charge carriers and extending their lifetime. Given the polycrystalline porous nature of the $SnO_2$ shells and their transparency to visible light, all parts of the nanoparticle are accessible: photons and chemical species in solution can easily access both the core and the shell parts of the nanoparticle. In a previous report, [23] we demonstrated the ability to modify the GS-NS@$SnO_2$ recipe to generate tin oxide shells doped with antimony and zinc simply by adding sodium antimonate and sodium zincate to the reaction mixture after the initial formation of $SnO_2$ seeds from sodium stannate. This strategy allows careful tuning of the conductivity, band gap, as well as the crystallinity of the semiconducting tin oxide shell in the core-shell $TiO_2$@$SnO_2$ nanoparticle system reported herein.

**Optical Properties:**

The optical properties were analyzed using UV-visible spectroscopy. Anatase $TiO_2$ has an optical band gap of ~3.2 eV while rutile $SnO_2$ has a band gap of 3.6-3.8 eV [8]. Notably, the UV absorption from $TiO_2$ is significantly more intense than that from $SnO_2$, as reported from theoretical calculations in previous literature [18]. A such, the UV-Vis spectra largely retain the features of $TiO_2$ core nanoparticles

after coating with the $SnO_2$ shell (see Figure 10). This result is also expected since the $TiO_2$ core is large (116 ± 43 nm) and is the major component even in the coated nanoparticles. However, the absorption increases at the lower wavelengths due to the contribution from the $SnO_2$ shell. Since both the band-gap and absorption of $SnO_2$ are lower than those of $TiO_2$, the band edge also is not affected after coating with $SnO_2$. These observations indicate that Sn is notdoped into the $TiO_2$ structure, but forms a separate $SnO_2$ phase instead, consistent with the XRD data. Notably, Meyer et al. have previously shown the possible formation of a mixed $Sn_xTi_yO_z$ interlayer between the $TiO_2$ and $SnO_2$ phases in the photoexcited state [15,36]. However, the dimensions of such an interlayer would be extremely small compared to the overall particle size. As such, any additional band-edge features would be negligible compared to the band gaps of the bulk phases and thus would not be observable in our UV-Vis spectra. Ultimately, further investigation using transient absorption spectroscopy and spectro-electrochemical studies can be undertaken to help elucidate the exact electronic mechanisms at the $TiO_2/SnO_2$ heterojunction.

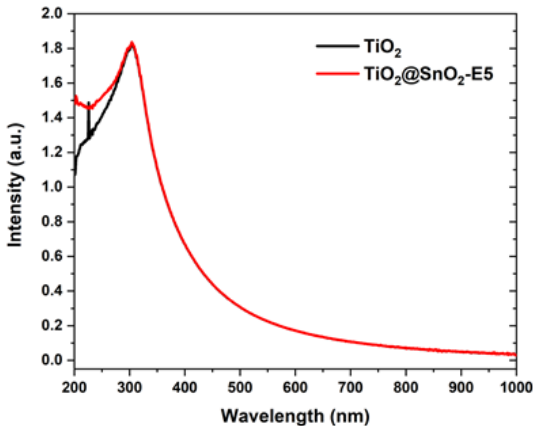


Figure 10. Extinction spectra for $TiO_2$@$SnO_2$-E5 core-shell nanoparticles, before and after coating with the $SnO_2$ shell.

## Conclusions

We demonstrated for the first time a strategy to fabricate type-II heterojunction of $TiO_2$ and $SnO_2$ in a core-shell nanoparticle system. The synthesis method utilizes a facile surfactant-free sodium stannate method to coat $SnO_2$ shells at ambient conditions on a metal oxide core. The synthesis method presents an effective strategy to localize $SnO_2$ crystallites on the surface of the $TiO_2$ cores and control the thickness of the $SnO_2$ shells between 5–40 nm, while limiting the formation of free $SnO_2$ nanoparticles. The synthesis method can also be adapted to synthesize thicker shells on metal cores, as well as embed nanoparticle cores within a network mesh of polycrystalline $SnO_2$ nanoparticles. The synthesis protocol can also be easily adapted to synthesize antimony- and zinc-doped tin oxide shells as shown in a previous study [23], providing the ability to further tune the electrical properties of the nanoscale heterojunction. The ability to fabricate the vital $TiO_2$@$SnO_2$ heterojunction in a colloidal nanoparticle allows utilization of their electrical properties in solution, in suspensions, dispersed in a matrix, or deposited as colloidal thin films. The $SnO_2$ shells are also expected to enhance the lifetime of photogenerated charge carriers in $TiO_2$, and vice versa. Combined with the ability to controllably vary the $SnO_2$ shell thickness [37] and to modulate the band gap of $SnO_2$ via doping, [23,24] this versatile $SnO_2$ coating method affords multiple handles to tune the electrical properties of semiconducting nanoparticles. On the whole, a combination of these optical and electrical properties should render these unique hybrid particles effective materials for photovoltaics, photocatalysis, optoelectronic devices, sensors, and Li-ion batteries.

**ORCID:** Riddhiman Medhi: 0000-0002-2368-2468

Nhat Ngo: 0000-0001-5710-1601

Tai-Chou Lee: 0000-0002-1695-1201

T. Randall Lee: 0000-0001-9584-8861

**Acknowledgement:** We thank the Air Force Office of Scientific Research (AFOSRFA9550-20-1-0349; 20RT0302), the Robert A. Welch Foundation (Grant Nos. E-1320), and the Texas Center for Superconductivity for generously supporting this research.

**Competing interests:** The authors report no conflict of interest.

## References

1. Dey, A. (2018). Semiconductor Metal Oxide Gas Sensors: A Review. *Mater. Sci. Eng. B, 229* 206–217.
2. Ray, C.; Pal, T. (2017). Recent Advances of Metal–Metal Oxide Nanocomposites and their Tailored Nanostructures in Numerous Catalytic Applications. *J. Mater. Chem. A, 5* (20), 9465–9487.
3. Yu, X.; Marks, T. J.; Facchetti, A. (2016). Metal Oxides for Optoelectronic Applications. *Nat. Mater.*, 15 383.
4. Liu, Y.; Wang, W.; Xu, X.; Marcel Veder, J.-P.; Shao, Z. (2019). Recent Advances in Anion-Doped Metal Oxides for Catalytic Applications. *J. Mater. Chem. A, 7* (13), 7280–7300.
5. Raghunath, A.; Perumal, E. (2017). Metal Oxide Nanoparticles as Antimicrobial Agents: A Promise for the Future. *Int. J. Antimicrob. Agents, 49* (2), 137–152.
6. Daghrir, R.; Drogui, P.; Robert, D. (2013). Modified $TiO_2$ For Environmental Photocatalytic Applications: A Review. *Ind. Eng. Chem. Res., 52* (10), 3581–3599.
7. Ganguly, A.; Anjaneyulu, O.; Ojha, K.; Ganguli, A. K. (2015). Oxide-Based Nanostructures for Photocatalytic and Electrocatalytic Applications. *CrystEngComm, 17* (47), 8978–9001.
8. Medhi, R.; Marquez, M. D.; Lee, T. R. (2020). Visible-Light-Active Doped Metal Oxide Nanoparticles: Review of their Synthesis, Properties, and Applications. *ACS Appl. Nano Mater., 3* (7), 6156–6185.
9. Chen, Y.-T.; Medhi, R.; Nekrashevich, I.; Litvinov, D.; Xu, S.; Lee, T. R. (2018). Specific Detection of Proteins Using Exceptionally Responsive Magnetic Particles. *Anal. Chem., 90* (11), 6749–6756.
10. Yi, Z.; Han, Q.; Zan, P.; Cheng, Y.; Wu, Y.; Wang, L. (2016). Facile fabrication of $SnO_2$@$TiO_2$ core–shell structures as anode materials for lithium-ion batteries. *J. Mater. Chem. A, 4* (33), 12850–12857.
11. Mazierski, P.; Mikolajczyk, A.; Bajorowicz, B.; Malankowska, A.; Zaleska-Medynska, A.; Nadolna, J. (2018). The Role of Lanthanides in $TiO_2$-Based Photocatalysis: A Review. *Appl. Catal. B-Environ., 233* 301–317.
12. Li, C.-H.; Li, M.-C.; Liu, S.-P.; Jamison, A. C.; Lee, D.; Lee, T. R.; Lee, T.-C. (2016). Plasmonically Enhanced Photocatalytic Hydrogen Production from Water: The Critical Role of Tunable Surface Plasmon Resonance from Gold–Silver Nanoshells. *ACS Appl. Mater. Interfaces, 8* (14), 9152–9161.
13. Ohtani, B. (2013). Titania Photocatalysis beyond Recombination: A Critical Review. *Catalysts, 3* (4), 942–953.
14. McCool, N. S.; Swierk, J. R.; Nemes, C. T.; Schmuttenmaer, C. A.; Mallouk, T. E. (2016). Dynamics of Electron Injection in $SnO_2/TiO_2$ Core/Shell Electrodes for Water-Splitting Dye-Sensitized Photoelectrochemical Cells. *J. Phys. Chem. Lett., 7* (15), 2930–2934.

15. Troian-Gautier, L.; Sampaio, R. N.; Piechota, E. J.; Brady, M. D.; Meyer, G. J. (2018). Barriers for Interfacial Back-Electron Transfer: A Comparison between $TiO_2$ and $SnO_2/TiO_2$ Core/Shell Structures. *J. Chem. Phys., 150* (4), 041719.
16. Gish, M. K.; Lapides, A. M.; Brennaman, M. K.; Templeton, J. L.; Meyer, T. J.; Papanikolas, J. M. (2016). Ultrafast Recombination Dynamics in Dye-Sensitized $SnO_2/TiO_2$ Core/Shell Films. *J. Phys. Chem. Lett., 7* (24), 5297–5301.
17. Martínez-Denegri, G.; Colodrero, S.; Kramarenko, M.; Martorell, J. (2018). All-Nanoparticle $SnO_2/TiO_2$ Electron-Transporting Layers Processed at Low Temperature for Efficient Thin-Film Perovskite Solar Cells. *ACS Appl. Energy Mater., 1* (10), 5548–5556.
18. Dou, M.; Persson, C. (2013). Comparative Study of Rutile and Anatase $SnO_2$ and $TiO_2$: Band-Edge Structures, Dielectric Functions, and Polaron Effects. *J. Appl. Phys., 113* (8), 083703.
19. Wang, C.; Shao, C.; Zhang, X.; Liu, Y. (2009). $SnO_2$ Nanostructures-$TiO_2$ Nanofibers Heterostructures: Controlled Fabrication and High Photocatalytic Properties. *Inorg. Chem., 48* (15), 7261–7268.
20. Huang, X.; Shang, L.; Chen, S.; Xia, J.; Qi, X.; Wang, X.; Zhang, T.; Meng, X.-M. (2013). Type-II ZnO Nanorod–$SnO_2$ Nanoparticle Heterostructures: Characterization of Structural, Optical and Photocatalytic Properties. *Nanoscale, 5* (9), 3828–3833.
21. Vinodgopal, K.; Bedja, I.; Kamat, P. V. (1996). Nanostructured Semiconductor Films for Photocatalysis. Photoelectrochemical Behavior of $SnO_2/TiO_2$ Composite Systems and Its Role in Photocatalytic Degradation of a Textile Azo Dye. *Chem. Mater., 8* (8), 2180–2187.
22. Khantamat, O.; Li, C.-H.; Liu, S.-P.; Liu, T.; Lee, H. J.; Zenasni, O.; Lee, T.-C.; Cai, C.; Lee, T. R. (2018). Broadening the Photoresponsive Activity of Anatase Titanium Dioxide Particles via Decoration with Partial Gold Shells. *J. Colloid Interface Sci., 513* 715–725.
23. Medhi, R.; Li, C.-H.; Lee, S. H.; Srinoi, P.; Marquez, M. D.; Robles-Hernandez, F.; Jacobson, A. J.; Lee, T.-C.; Lee, T. R. (2020). Antimony- and Zinc-Doped Tin Oxide Shells Coated on Gold Nanoparticles and Gold–Silver Nanoshells Having Tunable Extinctions for Sensing and Photonic Applications. *ACS Appl. Nano Mater., 3* (9), 8958–8971.
24. Medhi, R.; Li, C.-H.; Lee, S. H.; Marquez, M. D.; Jacobson, A. J.; Lee, T.-C.; Lee, T. R. (2019). Uniformly Spherical and Monodisperse Antimony- and Zinc-Doped Tin Oxide Nanoparticles for Optical and Electronic Applications. *ACS Appl. Nano Mater., 2* (10), 6554–6564.
25. Rai, D.; Yui, M.; Schaef, H. T.; Kitamura, A. (2011). Thermodynamic Model for SnO2(cr) and SnO2(am) Solubility in the Aqueous Na+–H+–OH—Cl—H2O System. *J. Solution Chem., 40* (7), 1155.
26. Choi, Y.-I.; Salman, S.; Kuroda, K.; Okido, M. (2013). Synergistic Corrosion Protection for AZ31 Mg Alloy by Anodizing and Stannate Post-Sealing Treatments. *Electrochim. Acta,* 97 313–319.
27. Oldfield, G.; Ung, T.; Mulvaney, P. (2000). Au@$SnO_2$ Core–Shell Nanocapacitors. *Adv. Mater., 12* (20), 1519–1522.
28. Zhang, D.; Jing, F.; Gao, F.; Shen, L.; Sun, D.; Zhou, J.; Chen, Y.; Ruan, S. (2015). Enhanced Performance of a $TiO_2$ Ultraviolet Detector Modified with Graphene Oxide. *RSC Adv., 5* (102), 83795–83800.
29. Zhu, H.; Tao, J.; Dong, X. (2010). Preparation and Photoelectrochemical Activity of Cr-Doped $TiO_2$ Nanorods with Nanocavities. *J. Phys. Chem. C, 114* (7), 2873–2879.
30. Lee, J.-W.; Kong, S.; Kim, W.-S.; Kim, J. (2007). Preparation and Characterization of $SiO_2/TiO_2$ Core-Shell Particles with Controlled Shell Thickness. Mater. *Chem. Phys., 106* (1), 39–44.
31. Andrulevičius, M.; Tamulevičius, S.; Gnatyuk, Y.; Vityuk, N.; Smirnova, N.; Eremenko, A. (2008). XPS Investigation of $TiO_2/ZrO_2/SiO_2$ Films Modified with Ag/Au Nanoparticles. *Mater. Sci. Medzg., 14* (1), 8–14.
32. Sheng, J.; Tong, H.; Xu, H.; Tang, C. (2016). Preparation and Photocatalytic Activity of $SnO_2$@$TiO_2$ Core–Shell Composites Modified by Ag. *Catal. Surv. Asia, 20* (3), 167–172.
33. Kumar, A.; Rout, L.; Achary, L. S. K.; Mohanty, A.; Dhaka, R. S.; Dash, P. (2016). An Investigation into the Solar Light-Driven Enhanced Photocatalytic Properties of a Graphene Oxide–$SnO_2$–$TiO_2$ Ternary Nanocomposite. *RSC Adv., 6* (38), 32074–32088.
34. Yang, Z.; Lu, X.; Tan, W.; Zhao, J.; Yang, D.; Yang, Y.; He, Y.; Zhou, K. (2018). XPS Studies of Nitrogen Doping Niobium used for Accelerator Applications. *Appl. Surf. Sci*., 439 1119–1126.
35. Gilbert, J. B.; Rubner, M. F.; Cohen, R. E. (2013). Depth-Profiling X-Ray Photoelectron Spectroscopy (XPS) Analysis of Interlayer Diffusion in Polyelectrolyte Multilayers. *Proc. Natl. Acad. Sci., 110* (17), 6651.
36. James, E. M.; Barr, T. J.; Meyer, G. J. Evidence for an Electronic State at the Interface between the $SnO_2$ Core and the $TiO_2$ Shell in Mesoporous $SnO_2/TiO_2$ Thin Films. *ACS Appl. Energy Mater*. 2018, 1, 859–867.
37. Srinoi, P.; Marquez, M. D.; Lee, T.-C.; Lee, T. R. (2020). Hollow Gold-Silver Nanoshells Coated with Ultrathin $SiO_2$ Shells for Plasmon-Enhanced Photocatalytic Applications. *Materials, 13* (21), 4967.